

Measuring the velocity field of a shear-coaxial, cryogenic flame in a high-pressure rocket thrust chamber

Min Son^{a,*}, Wolfgang Armbruster^a, Justin S. Hardi^a,
Michael Oswald^{a,b}

^aDLR Institute of Space Propulsion, Im Langen Grund, 74239 Hardthausen, Germany

^bInstitute of Jet Propulsion and Turbomachinery, RWTH Aachen University, Templergraben 55, 52062 Aachen, Germany

Received 7 November 2019; accepted 19 July 2020

Available online 19 September 2020

Abstract

High-speed imaging was used to visualize one of the transcritical flames in a multi-injector, sub-scale rocket thrust chamber at pressures up to 80 bar. Image correlation velocimetry (ICV) was applied to the imaging to obtain quantitative information on the flow field from the shear-coaxial injectors. ICV was used to track surface irregularities on the liquid oxygen (LOX) jet in imaging filtered to blue wavelengths. By choosing the interrogation area carefully, only the LOX jet was effectively tracked, excluding the coaxial H₂ flow, and the time-averaged velocity field was reconstructed. Due to the transient nature of the tracked features, which frequently change shape or disappear, the averaged ICV result underestimates the absolute values of velocity. Therefore, the averaged values were scaled by the mean of the instantaneous velocity maxima. A second, reference measurement of LOX jet propagation speed was calculated using dynamic mode decomposition (DMD). The results were consistent following the aforementioned correction of the ICV values. Comparing the ICV fields for two different operating conditions showed a marked difference in the axial velocity distribution and lateral expansion of the LOX jet, demonstrating the potential of the method in studying injection in rocket combustion chambers.

© 2020 The Authors. Published by Elsevier Inc. on behalf of The Combustion Institute.

This is an open access article under the CC BY-NC-ND license

(<http://creativecommons.org/licenses/by-nc-nd/4.0/>)

Keywords: Liquid rocket engine; Transcritical injection; Flame visualization; Image correlation velocimetry

1. Introduction

The design of injectors for cryogenic rocket engines is commonly based on empirical rules derived from full-scale engine performance measurements

or non-reacting fluid dynamic experiments [1]. The consequence is that dynamic characteristics of a thrust chamber can be poorly predicted, and other problems like combustion instabilities are persistently faced by developers of new engines, even in those using mature injector technology such as the classical shear-coaxial type for cryogenic propellant combinations such as LOX/H₂ or LOX/CH₄. Experimentally derived contributions to under-

* Corresponding author.

E-mail address: min.son@dlr.de (M. Son).

standing injection phenomenology or flame dynamics under conditions representative of rocket engines are rare. While contributions from numerical modelling are continuously improving in fidelity and accuracy [2,3], CFD methods are yet to reach the status of a definitive design tool. Since experiments under realistic, rocket-like conditions are rare, the availability of data suitable for validation purposes is likewise rare.

Optical diagnostics generate highly valued data for comparison with numerical results. However, the very high temperatures and pressures in rocket combustion chambers make their application very challenging. Techniques commonly achievable in rocket combustion fields are shadowgraph and filtered flame radiation imaging. Some early examples from experiments with shear coaxial injectors and LOX/H₂ or LOX/CH₄ are from Mayer and Tamura [4], Kendrick et al. [5], Juniper et al. [6], and Candel et al. [7]. They were able to characterize the LOX jet disintegration, shear layer, and extent of the flame, under pressures reaching into the supercritical regime for O₂.

The application of quantitative techniques is scarce indeed. Singla et al. applied PLIF to supercritical [8] and subcritical [9] flames, but faced difficulties due to the high temperatures and density gradients in these types of flames. The same problem complicates temperature and H₂O concentration measurements with CARS [10,11]. At lower pressures of around 10 bar, Fdida et al. [12] attained velocity field measurements using particle tracking velocimetry on LOX droplets in shadowgraph imaging of a spray flame. At higher pressures there are no droplets to track and no method to seed a reacting cryogenic flow with particles for PIV.

In rocket combustion instability experiments, the dynamic response of flames to acoustic fields has also been visualized, with some attempts to extract quantitative measurements. For example, Richecoeur et al. [13] reconstructed artificial streamlines from a motion tracking method and showed the flame movement was affected by forced transverse acoustic excitation. Hardi et al. [14] measured the intact LOX core length relative to the amplitude of forced transverse acoustic resonance at supercritical pressure. Roa and Talley [15] tracked local peaks of OH* radiation in the shear layer and derived the mean velocity of the flame front. Foust et al. [16] used a PIV method with Al₂O₃ particles to measure the velocity field of a rocket-like GH₂/GO₂ flame under 1.29 MPa chamber pressure. However, to the authors' knowledge, there have been no attempts to measure velocities of the LOX jet. LOX jet dynamics are known to play an important role in combustion instabilities [17,18], and so a database of velocity measurements would be of particular value to phenomenological understanding and for validating models.

In the present study, an image correlation velocimetry (ICV) technique was used to extract the velocity distribution of the LOX jet from a sub-scale LOX/H₂ rocket thrust chamber operating up to 80 bar. Filtered blue radiation imaging from the 42-injector combustor by Armbruster et al. [18] showed good resolution of periodic modulation of the LOX jet, and so they isolated and studied it with dynamic mode decomposition (DMD). In this work, ICV was applied to the same blue radiation imaging to track the periodic features on the LOX jet.

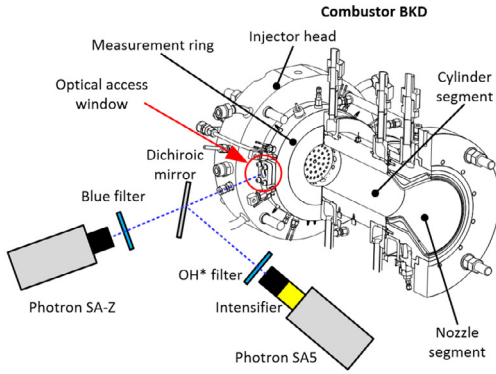
In this paper, the application of the ICV method is described, including a sensitivity study leading to optimized parameter selection. A correction method is introduced to improve the accuracy of absolute velocity values, and the corrected values are validated against a second measurement method based on the analysis of DMD modes. Then, velocity field results are compared between two operating conditions, one with stable combustion, and one with coupled resonance of the combustion chamber and injector acoustic modes.

2. Experimental setup

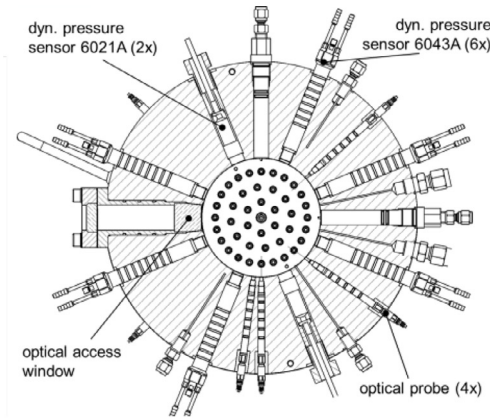
The research combustor model 'D' (abbr. BKD), as shown in Fig. 1a, is a sub-scale thrust chamber used by Armbruster et al. [18] to study self-excited combustion instabilities with flame visualization. BKD has 42 shear-coaxial injectors, which have a 3.6 mm LOX post inner diameter and 0.2 mm post thickness with 2 mm recess, and 4.5 mm outer diameter H₂ sleeve.

BKD has an instrumented measurement ring to obtain optical and acoustical data as shown in Fig. 1b. Filtered OH* and blue radiation were captured through the optical access window by high-speed cameras with filters; 310 ± 5 nm for OH* and 436 ± 5 nm for blue radiation as shown in Fig. 1a. They were afforded a view of the first 18 mm of one of the flames in the outer row of injectors as illustrated in Fig. 2. Only the blue imaging was analyzed in this study due to the resolution of the LOX jet. It was captured with 60,000 frames per second and the image resolution was approximately 0.15 mm/pixel. More detail on the optical setup is given by Armbruster et al. [18].

Armbruster et al. considered the two operating conditions, or 'load points' (LPs), given in Table 1. LP1 is the lower chamber pressure (P_{cc}) condition and is considered stable because it has only weak coupling between injector resonances and the transverse acoustic mode in the chamber, and correspondingly low unsteady pressure amplitude. LP2 is a high-pressure LP with stronger resonant coupling. Both LPs have a similar ratio of oxidizer to fuel mass flow rate (ROF). As shown in the spectrogram in Fig. 3, while the second longitudinal mode of the LOX post (LOX 2L) was de-



(a) Cut view of combustor and optical diagnostics setup



(b) Cross section of measurement ring

Fig. 1. Research combustor model 'D' (BKD) [18].

coupled from the first transverse mode of combustion chamber (CC 1T) for LP1, both were coupled at around 10 kHz for LP2. This coupling raises the chamber pressure fluctuations (p') to around $\pm 2.5\%$ of P_{cc} , evident in Fig. 3, which is close to the conventional classification for combustion instability.

The injection velocity of propellants is usually estimated simply as the volumetric flow rate divided by the injector area, where the fluid state

Table 1
Load points and conditions.

Load point	LP1	LP2
P_{cc} (bar)	51.8 ± 0.67	81.7 ± 1.06
ROF	5.0 ± 0.2	4.9 ± 0.2
$T_{inj, LOX}$ (K)	114 ± 3.43	113 ± 3.38
T_{inj, H_2} (K)	103 ± 3.08	103 ± 3.10
$u_{0, LOX}$ (m/s)	7.4 ± 0.22	11.5 ± 0.36
u_{0, H_2} (m/s)	400 ± 17.8	417 ± 18.8
J	35 ± 3.4	23 ± 2.3

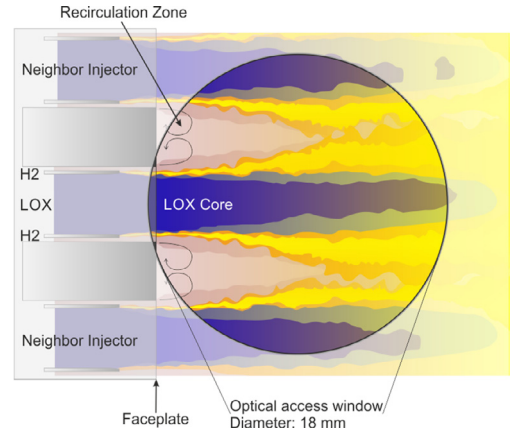


Fig. 2. Visualized region near injector plate.

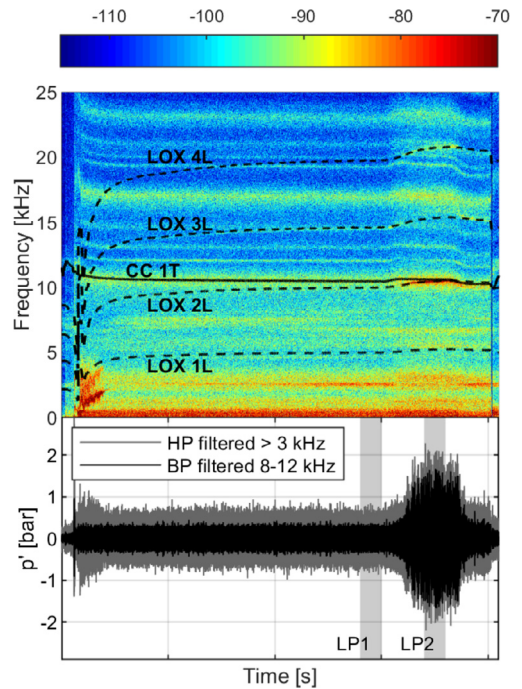


Fig. 3. Spectrogram (upper) and chamber pressure fluctuation p' (lower) for two load points [18].

is taken at P_{cc} and the temperature measured upstream in the injector distribution manifold (T_{inj}). The LOX injection velocity ($u_{0, LOX}$) was around 10 m/s, while for H_2 (u_{0, H_2}) it was around 400 m/s. This results in values of momentum flux ratio ($J = \rho_{H_2} u_{0, H_2}^2 / \rho_{LOX} u_{0, LOX}^2$) for the LPs in the upper end of the range common for LOX/ H_2 rocket engines. The main contributions to measurement uncertainties are from the mass flow meters with $\pm 3\%$, static

pressure sensors with ± 1 -1.3%, and ± 2.5 -3% for thermocouples at cryogenic temperature.

3. Analysis methods and results

3.1. Velocity measurement from DMD mode

In previous work, Armbruster et al. [18] identified and isolated LOX jet dynamics in the blue imaging using DMD. Here, a LOX propagation velocity distribution will be extracted from the DMD mode and used as a reference measurement.

In BKD, the flame is known to oscillate at frequencies corresponding to the resonance modes of the LOX injection tubes, or LOX posts [17]. Armbruster et al. visualized this effect and found that, in the blue imaging, it manifests as a pulsating LOX injection stream, and that the convection of periodically injected LOX 'lumps' with the bulk of the jet could be described in a strongly coherent DMD mode.

The mode capturing the LOX 1L response at around 5 kHz (indicated in Fig. 3), is shown in Fig. 4, with a wavy horizontal structure. The propagation of these waves in the reconstructed DMD mode is taken to represent the bulk convection velocity, filtered at the LOX post resonance frequency. The distance between intensity peaks, Δx (right side of Fig. 4) was measured at regular axial positions along the centreline and transformed to a local value of axial velocity (u_{DMD}) with the known image size, mode frequency and phase difference.

The u_{DMD} profile for LP2 is shown in Fig. 5. It can be considered as a distribution of averaged axial velocity, since the DMD mode describes the mean spatial dynamics. The error bars are calculated assuming that the uncertainty has a rectangular distribution [19]. The maximum value, $u_{DMD,max}$, was approximately 35.7 ± 2.4 m/s and appeared at 1.15 and 1.54 normalized axial distances from the injector plate, x/D_O , where D_O is the LOX post inner diameter.

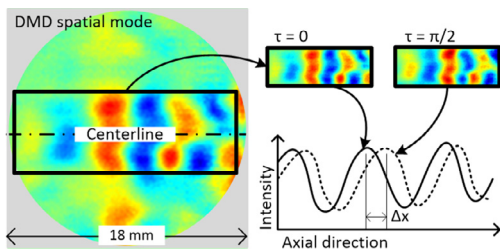


Fig. 4. Measurement of LOX jet velocity from DMD mode.

3.2. Velocity measurement from ICV

Usually, PIV methods are used in combustion research to measure flow velocity fields using seeding particles such as silicon dioxide [20]. However, seeding particles do not survive the conditions of LOX/H₂ combustion under high pressure. Owing to the low self-absorption characteristic of blue radiation, the LOX jet structure at the core of the flame is revealed by the shadow it casts from blocking illumination from its own far side, and from the multitude of flames behind it as shown in Fig. 6. Larger accumulations of LOX appear darker and their peripheries are well highlighted by the radiating mixing layer surrounding them. Thus, the visualized jet lumps in the blue radiation images could be used as tracers.

In principle, PIV algorithms can track any movement of structures in an image series based on cross correlation, known as image correlation velocimetry (ICV). In this work, ICV was used to track LOX jet movement in the blue radiation im-

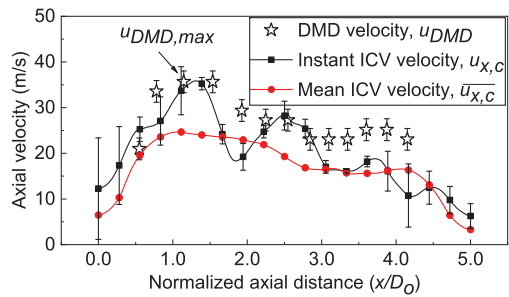


Fig. 5. Axial velocity profiles from DMD and ICV (LP2).

-  Darker jet lumps
-  Calculated vector from jet lumps

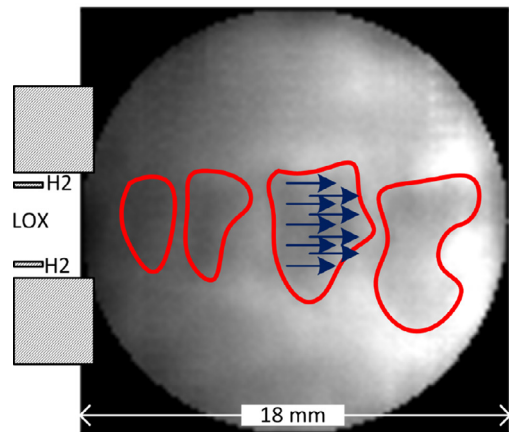


Fig. 6. Tracking parcels of LOX jet from blue radiation by ICV.

ages by cross correlation. The LOX jet itself is longer than the extent of the optical access. According to measurements by Hardi et al. from another combustor of similar scale and operating conditions, the intact LOX jet length is inversely proportional to chamber pressure fluctuations (p') normalized by P_{cc} [14]. When p'/P_{cc} is 2.5% for LP2, the average jet length in BKD is expected to be approximately 72 mm. This is much longer than the optical window size of 18 mm, and so it is structures on the surface of, or shed from, the LOX jet which can serve as tracers within the window region.

With the very high frame rate of 60,000 fps, the bulky LOX structures survive long enough to be tracked by ICV with certainty before they deform beyond recognition or are consumed by the flame. An impression of the tracers' form and consistency can be obtained from the DMD result in Fig. 4. In the spatial mode, vertical columns of fluctuating intensity arranged near the centerline are observed. Since LOX lumps appear in the blue image as darker regions as shown in Fig. 6, their form corresponds to regions of negative intensity fluctuation (blue) in the DMD spatial mode. Their prominence in the DMD mode indicates statistical consistency in the behavior of these shapes, and that they maintain their form from the injection plane to around 12 mm downstream, which is around 2/3 of the window size. Based on the DMD velocity, the tracer lifetime can be estimated to be around 0.5 ms. With a 0.017-ms delay between frames at 60 kfps, this lifetime is sufficient for tracers to be tracked for many sequential frames by ICV.

The algorithm used in this study was proposed by Thielicke and Stamhuis [21], and uses advanced discrete Fourier transform to increase the accuracy of the cross-correlation. Additionally, to improve the accuracy in non-uniform particle motion, multiple passes of interrogation areas (IAs) with different sizes are used and the velocity vector is sequentially corrected for decreasing IAs. A rule to ensure vector accuracy is that particle displacement between snapshots should be less than one quarter of the smallest IA. A smoothing method and rejection of erroneous detections were applied after constructing the vector fields. Rejected vectors had velocity values exceeding the standard deviation of the mean for the instantaneous vector field by a factor of seven [21], and amounted to less than 1% of total vectors. This reduces systematic errors but retains dynamical characteristics interesting for future study.

The LOX jet displacement in BKD imaging was estimated from $u_{0,LOX}$ and the imaging frame rate. As shown in Table 1, $u_{0,LOX}$ was around 10 m/s and u_{0,H_2} around 400 m/s. These were taken as reference velocities, and expressed as pixel per frame (px/fr) values with 1.1 px/fr for LOX and 44.4 px/fr for H_2 . To determine an appropriate size of the search area, IA, Keane and Adrian recommended that a parti-

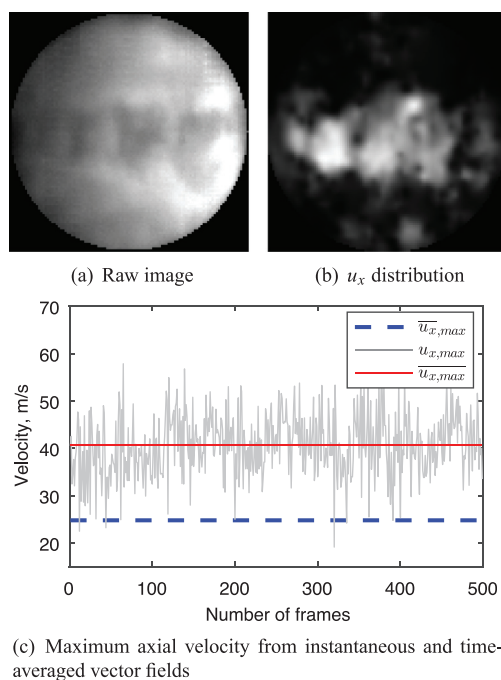
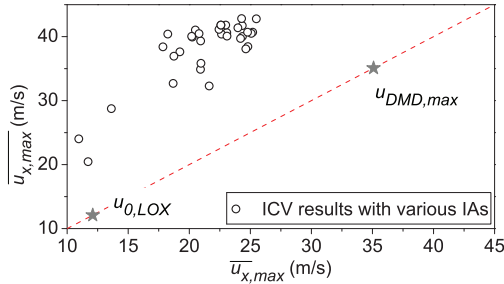


Fig. 7. ICV results for LP2.

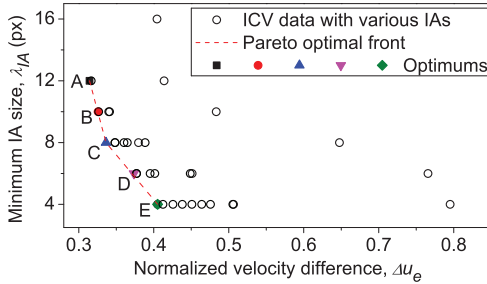
cle displacement should not exceed 25% of IA [22]. Thus if the IAs were chosen between approximately 4×4 which is about 4 times larger than the LOX pixel velocity and 32×32 which is less than the H_2 pixel velocity, the LOX jet could be tracked while excluding any influence of the faster H_2 flow.

While the injected LOX jet is ideally envisaged as a continuous, smooth jet, the real combustion field in the experiment is unsteady and turbulent. Therefore, periodic and lumpy structures on the LOX jet are visible in the raw imaging, for example in the instantaneous blue radiation image from LP2 in Fig. 7a. The jet is not interrupted, but structures have a somewhat isolated appearance because heightened radiation intensity separates the regions of accumulated LOX. Regardless, these structures could be tracked by ICV, as shown in the instantaneous axial (x-component) velocity field result in Fig. 7b. However, due to the lack of a uniform seeding field to track and fragmentation of the LOX jet as shown in Fig. 7a, the resulting velocity field is modulated by the interruption of tracked structures. This is evident in the instantaneous velocity profile extracted from the image center line of Fig. 7b, $u_{x,c}$, and plotted in Fig. 5. The error bars in instantaneous velocity were calculated based on the interrogation window settings used for ICV described in Section 3.6. In some regions the values agree well with u_{DMD} , while in others there are sudden troughs.

This discontinuous tracking complicates the derivation of a time-averaged field. Time-averaged



(a) Velocity results at various IAs



(b) Pareto optimum

Fig. 8. Sensitivity of results on IA (LP2).

velocity values were around 1/3 lower than in the instantaneous fields and u_{DMD} , as illustrated by the center-line profile from the time-averaged field, $\overline{u_{x,c}}$, shown in Fig. 5. In the case of LP2, the maximum velocity in the time-averaged field, $\overline{u_{x,max}}$, was around 25 m/s, whereas the average of the maximum velocity in each instantaneous field, $\overline{u_{x,max}}$, was around 40 m/s as shown in Fig. 7c. In a later section, $\overline{u_{x,max}}$ will be used as the correction factor to compensate the non-homogeneous tracking problem.

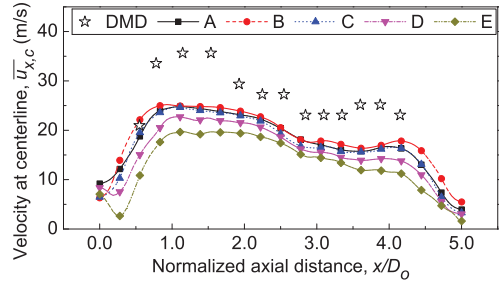
3.3. Sensitivity of ICV parameters

The combination of IA values in the multi-pass ICV algorithm was varied to study the sensitivity of the results on the choice of parameters and to seek an optimum setting. The sizing of IA was varied between 32 and 4 pixels, with the IA decreasing between passes. The minimum IA of 4 resulted in the highest vector field resolution.

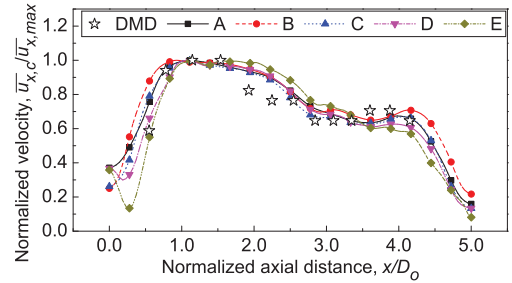
The difference between $\overline{u_{x,max}}$ and $\overline{u_{x,max}}$ were affected by the IA parameters, as can be seen in Fig. 8a. Considering the DMD result as the reference value, the ICV results closest to the reference were taken to be the best choice of IAs. Hence, a multi-objective optimization problem was formulated with the following two objectives; minimizing the IA for the last pass, λ_{IA} , for best resolution, and minimizing the Euclidean distance between the

Table 2
Optimal IA parameter cases.

Case	Multi-pass IAs	Δu_e	λ_{IA}
A	32-16-12	0.314	12
B	32-16-12-10	0.326	10
C	32-16-12-8	0.336	8
D	32-16-12-6	0.374	6
E	16-10-4	0.405	4



(a) Original velocity



(b) Normalized velocity

Fig. 9. $\overline{u_c}$ for the optimal cases (LP2).

ICV and DMD points, Δu_e , calculated as

$$\left[(u_{DMD,max} - \overline{u_{x,max}})^2 + (u_{DMD,max} - \overline{u_{x,max}})^2 \right]^{0.5} \tag{1}$$

The two objectives for all cases in Fig. 8a were plotted in Fig. 8b, and the Pareto optimal front was also derived. In multi-objective problems, multiple optimal cases can exist [23]. In the trade-off problem between the two objectives considered here, five optimal cases were obtained as listed in Table 2.

The averaged ICV center-line distributions ($\overline{u_{x,c}}$) for these cases were compared as shown in Fig. 9a. Globally, they lie below u_{DMD} . The profiles of cases A, B, and C are most similar to each other and have the highest resolution. They also follow the u_{DMD} profile most closely, as shown by the overlay of normalized profiles in Fig. 9b. Of these, case C had the lowest mean difference to the DMD profile, and also the lowest calculation overhead, and is therefore declared the best choice.

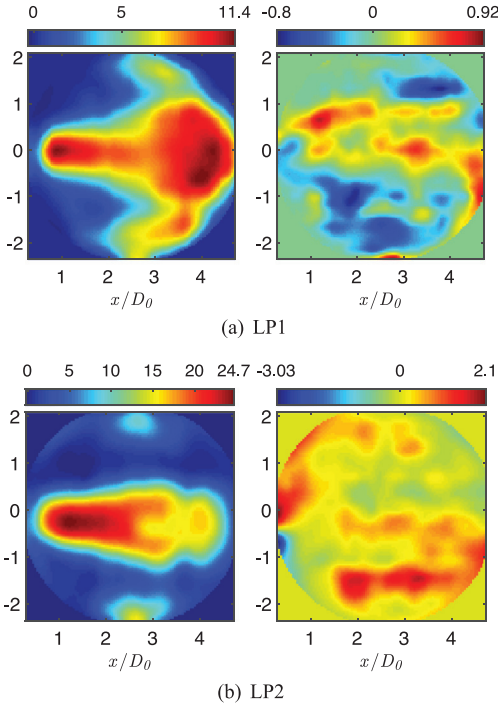


Fig. 10. Time-averaged contours of axial velocity ($\overline{u_x}$, left) and radial velocity ($\overline{u_r}$, right) (m/s) at two different load points.

3.4. ICV results

With the optimal choice of IA parameters from case C, the ICV analysis was performed with a series of 500 images from LP1 and LP2. The results are shown as averaged axial ($\overline{u_x}$) and radial ($\overline{u_r}$) velocity component distributions in Fig. 10. For both LPs, the $\overline{u_x}$ distributions are symmetric about the axis and appear to depict the progression of the LOX jet, whereas the H_2 flow is excluded. The $\overline{u_r}$ is comparatively small everywhere, meaning that the axial velocities are strongly dominant for the LOX jet. Uncertainty value distributions for \overline{u} were estimated as shown in Fig. 11 by using

$$u = \overline{u} \pm (t_{N-1,95\%})\delta/N^{0.5}, \quad (2)$$

where δ is the standard deviation, N is total number of images, and $t_{N-1,95\%}$ is the student-t distribution for a 95% confidence interval with $N - 1$ degrees of freedom. Even though there were strong fluctuations in the unsteady field, the time-averaged fields have less than ± 1.34 m/s uncertainty.

3.5. Correction of ICV velocity

The center-line profile of $\overline{u_x}$ ($\overline{u_{x,c}}$) for LP2 from Fig. 10b was already depicted in Fig. 5, where it was seen to lie at much lower absolute values than $u_{x,c}$ and u_{DMD} , while following a consistent profile.

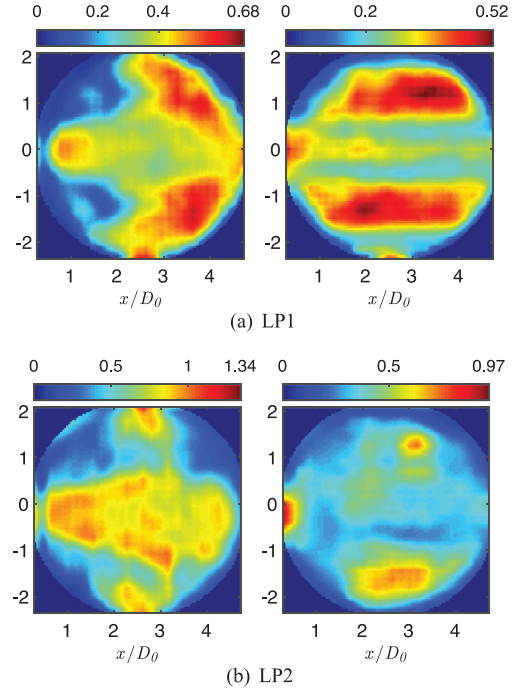


Fig. 11. Uncertainty contours of axial velocity ($\overline{u_x}$, left) and radial velocity ($\overline{u_r}$, right) (m/s) at two different load points.

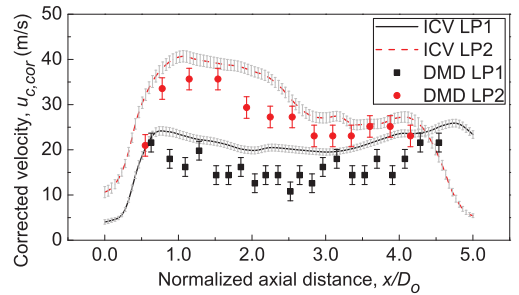


Fig. 12. Corrected axial velocity at the center line.

Therefore, a simple scaling of $\overline{u_{x,max}}/\overline{u_{x,max}}$ was performed to correct the absolute values from ICV. The corrected profiles of the LOX jet, $\overline{u_{c,cor}}$, are shown for LP1 and LP2 in Fig. 12. The uncertainty values for $\overline{u_{c,cor}}$ were also estimated by Eq. (2) and are presented in Fig. 12 as vertical error bars. After the correction, ICV results showed good agreement with DMD results.

3.6. Discussion of results

Following correction of the u_x values, the results from LP1 and LP2 can now be compared

and contrasted. It should be noted that velocity field results suffer from some optical distortion near the window edges. Feature tracking in these areas is also affected most strongly by the choice of IA parameters. This is particularly evident in the variation between optimal case profiles in Fig. 9b in the region from $x/D_O = 0.0$ to 0.5. In general, the results between roughly 0.8 and 4.5 are considered to be most reliable.

The first observation from Fig. 12 is that LP2 has higher absolute u_x values than LP1. This is consistent with the higher injected mass flow rate for LP2 and the initial estimates of $u_{0,LOX}$.

The peak values of u_x from both the ICV and DMD methods are about three times greater than $u_{0,LOX}$, suggesting that the common, simple way to evaluate $u_{0,LOX}$ significantly underestimates jet velocity values reached in the near injector region. This should be taken into consideration in low-order modelling or when analyzing LOX jet and flame dynamics.

Two main factors are hypothesized to contribute to this discrepancy. The first is the LOX density. The LOX is in fact in a supercritical state and is therefore not an incompressible fluid (Z approx. 0.3). Its temperature at the exit of injector is unknown, and could be raised by heat transfer along the narrow injector flow path. Therefore, the density at the injection plane could be lower than the usual estimate based on the last point of measurement in the upstream manifold. In addition, rapid heating of the LOX stream from combustion immediately after injection can also decrease the density in the combustion field. Thus, the factors increasing the LOX density can cause underestimation of the LOX injection velocity.

The second factor is acceleration of the LOX jet. The surface layers of the jet can be accelerated by the shear flow of the high-speed, coaxial H_2 stream, particularly in the recess region of the injector. Additionally, the LOX injector of BKD is recessed, and so the expanding H_2 flow can pinch the LOX jet, decreasing its effective injection area and increasing the jet speed. A detailed comparison with CFD simulation could help consolidate the contributions of such effects to the deficiency in $u_{0,LOX}$ values.

The $u_{c,cor}$ profiles for LP1 and LP2 in Fig. 12 differ from each other. For LP1, the LOX jet experienced slight deceleration up to x/D_O around 2.5 and then acceleration to values higher than at the start. In Fig. 10a, the phase of acceleration is accompanied by radial expansion of the LOX jet, to the extent that it begins to meet the LOX jets of the neighboring injection elements by about $x/D_O = 3.5$. On the other hand, the LP2 profile is characterised by two plateaus, separated by deceleration around $x/D_O = 2.5$. In Fig. 10b, the LOX jet appears to radially contract after this point, in contrast to the LP1 distribution.

Since these are the only velocity measurements in a transcritical, reacting flow known to the authors, an explanation of these flow field differences will be reserved for future work where it is hoped that comparison with CFD modeling can inform their physical interpretation.

At this point, the authors can only speculate on the contribution of injection parameters, fluid thermodynamic state, and LOX jet inflow modulation on the differences in ICV field structure. However, it is promising to see that the ICV analysis produced two markedly different results for the different LPs, which suggests that the approach can contribute valuable information to the study of injection and flame dynamics.

4. Conclusion

In this study, image correlation velocimetry (ICV) was used to extract quantitative estimates of the LOX jet velocity distribution in a high-pressure LOX/ H_2 flame in a rocket combustion chamber. To the authors' knowledge, these are the first two-dimensional velocity field measurements from a shear-coaxial flame at supercritical pressure.

The ICV routine was applied to high-speed imaging filtered to blue wavelengths without any kind of PIV seeding. The results showed that LOX jet surface irregularities could successfully be tracked and used as a measure of jet velocity. However, time-averaged velocity was underestimated due to the transient nature of the tracked features. Correcting the absolute values with the mean of the instantaneous velocity field maxima produced results consistent with reference measurements produced using dynamic mode decomposition (DMD). Due to the nature of the discontinuous field of the unsteady LOX jet, additional correction should be applied comparing the time-averaged velocity with the maximum velocity from instantaneous images. Nevertheless, the ICV can provide instantaneous and dynamic velocity information, while DMD is temporally filtered. While a demonstration of this capability is outside the scope of the current paper, we see great potential for its use in the dynamical analysis of imaging from such challenging experimental conditions.

A common, simplified way to estimate the injection velocity from rocket injectors is calculated from volumetric flow rate and fluid density estimated from an upstream temperature measurement and the downstream combustion chamber pressure. The LOX jet velocity measured with the image processing techniques in this study was higher than the simple estimate by around a factor of three. While further study is required to explain why, this is a significant finding which should be considered in all design, analysis or modeling activities involving an estimate of LOX injection velocity.

The velocity profiles were analyzed from two different operating conditions; one stable at near-critical combustion chamber pressure, and one with heightened injection dynamics at supercritical pressure. The resulting profiles indicate significantly different LOX jet structures and acceleration profiles between the two conditions. CFD modeling is needed to support interpretation of the results, but the fact of the clear contrast in velocity fields is promising. It suggests the ICV method can make valuable contributions to the further study of flame dynamics, and to the establishment of an experimental database for CFD validation.

Declaration of Competing Interest

The authors declare that they have no known competing financial interests or personal relationships that could have appeared to influence the work reported in this paper.

Acknowledgments

Financial support has been provided by the German Research Foundation (DFG) in the framework of the SFB TRR40 cooperative research center. The work is also associated with the French-German Rocket Engine Stability initiative (REST). The authors would like to thank the crew of the P8 test facility for test operations as well as Robert Stützer for setting up the optical diagnostics.

References

- [1] D. Huzel, D. Huang, *Modern Engineering For Design of Liquid-Propellant Rocket Engines*, Progress in Astronautics and Aeronautics, 147, AIAA, 1992.
- [2] D.T. Banuti, P.C. Ma, J.-P. Hickey, M. Ihme, *Combust. Flame* 196 (2018) 364–376.
- [3] G. Lacaze, J.C. Oefelein, *Combust. Flame* 159 (6) (2012) 2087–2103, doi:10.1016/j.combustflame.2012.02.003.
- [4] W. Mayer, H. Tamura, *J. Propuls. Power* 12 (6) (1996) 1137–1147.
- [5] D. Kendrick, G. Herding, P. Scoufflaire, C. Rolon, S. Candel, *Combust. Flame* 118 (3) (1999) 327–339.
- [6] M. Juniper, A. Tripathi, P. Scoufflaire, J.-C. Rolon, S. Candel, *Proc. Combust. Inst.* 28 (1) (2000) 1103–1109.
- [7] S. Candel, M. Juniper, G. Singla, P. Scoufflaire, C. Rolon, *Combust. Sci. Technol.* 178 (1–3) (2006) 161–192, doi:10.1080/00102200500292530.
- [8] G. Singla, P. Scoufflaire, C. Rolon, S. Candel, *Combust. Flame* 144 (1) (2006) 151–169.
- [9] G. Singla, P. Scoufflaire, C. Rolon, S. Candel, L. Vingert, *J. Propuls. Power* 23 (3) (2007) 593–602.
- [10] F. Grisch, P. Bouchardy, L. Vingert, W. Clauss, M. Oswald, V.V. Smirnov, Cars measurements at high pressure in cryogenic lox-gh2 jet flames, in: J. Hulka, M. Habiballah, V. Yang, M. Popp (Eds.), *Liquid Rocket Thrust Chambers: Aspects of Modeling, Analysis, and Design*, Progress in Astronautics and Aeronautics, 200, AIAA, Washington, DC, 2004.
- [11] W. Clauss, C. Manfretti, J. Sender, M. Oswald, V. Fabelinsky, V. Smirnov, O. Stel'makh, K. Vereschagin, in: 46th AIAA/ASME/SAE/ASEE Joint Propulsion Conference & Exhibit, AIAA 2010–7054, DLR, 2010, doi:10.2514/6.2010-7054. AIAA
- [12] N. Fdida, L. Vingert, A. Ristori, Y. Le Sant, *Atom. Sprays* 26 (5) (2016) 411–438.
- [13] F. Richecoeur, S. Ducruix, P. Scoufflaire, S. Candel, *Acta Astronaut.* 62 (1) (2008) 18–27.
- [14] J.S. Hardi, H.C.G. Martinez, M. Oswald, B.B. Dally, *J. Propuls. Power* 30 (2) (2014) 337–349.
- [15] M. Roa, D.G. Talley, *J. Propuls. Power* 35 (2) (2018) 369–381.
- [16] M. Foust, M. Deshpande, S. Pal, T. Ni, C. Merkle, R. Santoro, in: 34th Aerospace Sciences Meeting and Exhibit, 1996, p. 646.
- [17] S. Gröning, J.S. Hardi, D. Suslov, M. Oswald, *Journal of Propulsion and Power* (0) (2016) 560–573.
- [18] W. Armbruster, J.S. Hardi, D. Suslov, M. Oswald, *J. Propuls. Power* 35 (3) (2019) 632–644.
- [19] I. BIPM, I. IFCC, I. IUPAC, O. ISO, *Citado en las* 167 (2008).
- [20] C. Willert, M. Jarius, *Experiments in fluids* 33 (6) (2002) 931–939.
- [21] W. Thielicke, E. Stamhuis, *J. Open Res. Softw.* 2 (1) (2014).
- [22] R.D. Keane, R.J. Adrian, *Meas. Sci. Technol.* 1 (11) (1990) 1202.
- [23] M.K. Lotov A.V., in: J. Branke, J. Branke, K. Deb, K. Miettinen, R. Slowinski (Eds.), *Multiobjective Optimization: Interactive and Evolutionary Approaches*, 5252, Springer Science & Business Media, 2008, pp. 213–243.